J|A|C|S
ARTICLES

Size-Dependent Passivation Shell and Magnetic Properties in Antiferromagnetic/Ferrimagnetic Core/Shell MnO Nanoparticles

Alberto López-Ortega,[†] Dina Tobia,[‡] Elin Winkler,[‡] Igor V. Golosovsky,[§]
German Salazar-Alvarez,[†,||] Sònia Estradé,[⊥] Marta Estrader,*[,†] Jordi Sort,[¶,#]
Miguel Angel González,[@] Santiago Suriñach,[#] Jordi Arbiol,[¶,Δ] Francesca Peiró,[⊥]
Roberto D. Zysler,[‡] Maria Dolors Baró,[#] and Josep Nogués[¶,†]

*Centre d'Investigació en Nanociència i Nanotecnologia (ICN-CSIC), Campus Universitat
Autònoma de Barcelona, E-08193 Bellaterra, Spain, Centro Atómico Bariloche,
CNEA-CONICET, 8400 S.C. de Bariloche, Río Negro, Argentina, St. Petersburg Nuclear Physics
Institute, 188300 Gatchina, St. Petersburg, Russia, Department of Materials and Environmental
Chemistry, Stockholm University, S-10691 Stockholm, Sweden, MIND-IN2UB, Departament
d'Electrònica, Universitat de Barcelona, Martí i Franquès 1, E-08028 Barcelona, Spain,
Institució Catalana de Recerca i Estudis Avançats (ICREA), Barcelona, Spain, Departament de
Física, Universitat Autònoma de Barcelona, E-08193 Bellaterra, Spain, Institut Laue Langevin,
6 rue Jules Horowitz, BP 156, F-38042 Grenoble, France, and Institut de Ciència de Materials
de Barcelona (CSIC), Campus Universitat Autònoma de Barcelona, E-08193 Bellaterra, Spain*

Received March 15, 2010; E-mail: marta.estrader.icn@uab.cat

Abstract: The magnetic properties of bimagnetic core/shell nanoparticles consisting of an antiferromagnetic MnO core and a ferrimagnetic passivation shell have been investigated. It is found that the phase of the passivation shell (γ-Mn_2O_3 or Mn_3O_4) depends on the size of the nanoparticles. Structural and magnetic characterizations concur that while the smallest nanoparticles have a predominantly γ-Mn_2O_3 shell, larger ones have increasing amounts of Mn_3O_4. A considerable enhancement of the Néel temperature, T_N, and the magnetic anisotropy of the MnO core for decreasing core sizes has been observed. The size reduction also leads to other phenomena such as persistent magnetic moment in MnO up to high temperatures and an unusual temperature behavior of the magnetic domains.

Introduction

Magnetic nanoparticles are attracting a great deal of interest from both fundamental and applied points of view.[1−4] Magnetic recording media, catalysis, ferrofluids, pigments, hyperthermia, medical diagnostics, and drug delivery are among the increasing number of applications of magnetic nanoparticles. Due to their small size and, particularly, their large surface-to-volume ratio magnetic nanoparticles exhibit properties different from those of their bulk counterparts, which can be exploited to obtain new functionalities. Although ferromagnetic (FM) and ferrimagnetic (FiM) nanoparticles have been extensively studied, antiferromagnetic (AFM) nanoparticles have been far less investigated and are thus less understood.[5] Nevertheless, antiferromagnetic nanoparticles and nanostructures play an important role in spintronic devices[6] and have been proposed as means to overcome the superparamagnetic limit in recording media or to enhance the coercivity of ferromagnets.[7,8] Although finite size effects in antiferromagnetic nanoparticles are similar to those of FM or FiM materials (e.g., superparamagnetism or reduced blocking temperatures), some effects are specific to AFMs (e.g., the appearance of finite magnetization due to sublattice uncompensation).[1−5]

Special types of magnetic nanoparticles are core/shell nanoparticles. Although in most cases the shell serves just for protection purposes, the study of bimagnetic nanoparticles, where both the shell and the core are magnetic, is steadily increasing.[6,9−30] In fact, the shell properties and exchange coupling between the core and the shell open new degrees of

* To whom correspondence should be addressed: E-mail:
† ICN-CSIC, Campus Universitat Autònoma de Barcelona.
‡ CNEA-CONICET.
§ St. Petersburg Nuclear Physics Institute.
|| Stockholm University.
⊥ Universitat de Barcelona.
¶ ICREA, Universitat Autònoma de Barcelona.
# Departament de Física, Universitat Autònoma de Barcelona.
@ Institut Laue Langevin.
Δ Institut de Ciència de Materials de Barcelona (CSIC), Campus Universitat Autònoma de Barcelona.

(1) Lu, A. H.; Salabas, E. L.; Schuth, F. *Angew. Chem., Int. Ed.* **2007**, *46*, 1222–1244.
(2) Tartaj, P.; Morales, M. P.; Veintemillas-Verdager, S.; González-Carreño, T.; Serna, C. J. *J. Phys. D* **2003**, *36*, R182–R197.
(3) Batlle, X.; Labarta, A. *J. Phys. D* **2002**, *35*, R15–R42.
(4) Willard, M. A.; Kurihara, L. K.; Carpenter, E. E.; Calvin, S.; Harris, V. G. *Int. Mater. Rev.* **2004**, *49*, 125–170.

(5) Mørup, S.; Madsen, D. E.; Frandsen, C.; Bahl, C. R. H.; Hansen, M. F. *J. Phys.: Condens. Matter* **2007**, *19*, 213202.
(6) Nogués, J.; Sort, J.; Langlais, V.; Skumryev, V.; Suriñach, S.; Muñoz, J. S.; Baró, M. D. *Phys. Rep.* **2005**, *422*, 65–117.
(7) Skumryev, V.; Stoyanov, S.; Zhang, Y.; Hadjipanayis, G.; Givord, D.; Nogués, J. *Nature (London)* **2003**, *423*, 850–853.
(8) (a) Sort, J.; Suriñach, S.; Muñoz, J. S.; Baró, M. D.; Nogués, J.; Chouteau, G.; Skumryev, V.; Hadjipanayis, G. C. *Phys. Rev. B* **2002**, *65*, 174420. (b) Sort, J.; Nogués, J.; Suriñach, S.; Muñoz, J. S.; Baró, M. D.; Chappel, E.; Dupont, F.; Chonteau, G. *Appl. Phys. Lett.* **2001**, *79*, 1142–1144.

freedom to tailor the overall properties of the nanoparticles, leading to novel applications (such as enhanced coercivity and energy products, tunable blocking temperatures, improved electromagnetic radiation absorption, and hyperthermia treatment).[7,13,31−33] Core/shell nanoparticles with a FM (or FiM) core and a AFM (or FiM) shell have been widely investigated.[6,9−11] Recently, "inverse" core/shell nanoparticles, with AFM cores and FiM or spin-glass shells, have been synthesized, leading to a number of novel magnetic properties.[34−46] In particular, the magnetic properties of inverse core/shell nanoparticles based on the passivation of AFM MnO nanoparticles have been investigated.[34−38,40] These materials exhibit novel properties at low temperatures[34−37,40] such as very large exchange bias and coercivity with a nonmonotonic dependence on the core diameter[34] and spontaneous magnetization and ferrimagnetic order above the Curie temperature of the shell.[35−37] However, in these nanoparticles, although the shell material is usually identified as Mn_3O_4,[34,36−38,40] it has been recently shown that γ-Mn_2O_3 can also be formed as a result of MnO passivation.[35]

In this article we present the study of MnO (AFM)−γ-Mn_2O_3 or Mn_3O_4 (FiM) core/shell nanoparticles by diverse techniques (i.e., neutron diffraction, TEM, EELS, ac susceptibility, magnetometry, and electron spin resonance). The magnetic and structural results indicate that the structure of the passivation shell of the MnO nanoparticles depends on the core size, being primarily γ-Mn_2O_3 for small cores and progressively transforming to Mn_3O_4 for larger cores. Moreover, the core/shell nanoparticles exhibit a range of interesting properties such as large coercivities, exchange bias or enhanced anisotropy, and Néel temperatures of the core.

Experimental Section

Nanoparticles with different sizes were obtained by adding 7.5 mmol of manganese(II) acetylacetonate (Mn(acac)$_2$ purum, Aldrich) and 7.5 mmol of 1,2-hexadecanediol (HDD 90%, Aldrich) to 150 mL of dibenzyl ether (DBE analytical, Aldrich) in a 250 mL round-bottomed flask under an inert argon atmosphere followed by the addition of a surfactant, oleylamine (OA 70%, Aldrich), in a surfactant-to-metal ratio, [S]:[M] (mol/mol), from 1 to 40. The solution was mechanically stirred and heated, at a heating rate of 8−10 °C/min, to a given temperature, in the range of 190−240 °C with reflux and a residence time of 30−60 min. The flask was removed from the heating source, cooled in argon to 80 °C, and subsequently exposed to air and cooled to room temperature to obtain the passivated shell. The particles were washed from the reaction media by subsequent steps of precipitation under ethanol, centrifugation, and redispersion in hexane. The synthesis parameters are summarized in Table 1. **T1**

Neutron diffraction measurements were carried out at different temperatures, in the range 10−250 K, at the D20 diffractometer of the Institute Laue-Langevin with a neutron wavelength of 1.305 Å.[47] Typical neutron diffraction patterns are shown in Figure 1 **F1** and Figure S1 (Supporting Information). All diffraction patterns were analyzed using the FullProf code[48] based on the known crystal structures of MnO and γ-Mn_2O_3 (or Mn_3O_4). This method, in contrast with the so-called "matching mode", provides more stable refinement (see curve c in Figure 1 and Figure S1) in the present case due to the strong overlapping of the principal peaks and the presence of small parasitic reflections (see arrows in Figure 1). Note that the rather large diffuse background is due to the remains of surfactants used in the synthesis.

Transmission electron microscopy (TEM) images were obtained using a JEM-2010 instrument with a LaB$_6$ filament and a JEM-

(9) Iglesias, O.; Labarta, A.; Batlle, X. *J. Nanosci. Nanotechnol.* **2008**, *8*, 2761–2780.

(10) Liu, W.; Zhong, W.; Du, Y. W. *J. Nanosci. Nanotechnol.* **2008**, *8*, 2781–2792.

(11) Casavola, M.; Buonsanti, R.; Caputo, G.; Cozzoli, P. D. *Eur. J. Inorg. Chem.* **2008**, 837–854.

(12) Eftaxias, E.; Trohidou, K. N. *Phys. Rev. B* **2005**, *71*, 134406.

(13) Salazar-Alvarez, G.; Sort, J.; Uheida, A.; Muhammed, M.; Suriñach, S.; Baró, M. D.; Nogués, J. *J. Mater. Chem.* **2007**, *17*, 322–328.

(14) Liu, X. S.; Gu, B. X.; Zhong, W.; Jiang, H. Y.; Du, Y. W. *Appl. Phys. A: Mater. Sci. Process.* **2003**, *77*, 673–676.

(15) Zeng, H.; Sun, S.; Li, J.; Wang, Z. L.; Liu, J. P. *Appl. Phys. Lett.* **2004**, *85*, 792–794.

(16) Figuerola, A.; Fiore, A.; Di Corato, R.; Falqui, A.; Giannini, C.; Micotti, E.; Lascialfari, A.; Corti, M.; Cingolani, R.; Pellegrino, T.; Cozzoli, P. D.; Manna, L. *J. Am. Chem. Soc.* **2008**, *130*, 1477–1487.

(17) Nogués, J.; Skumryev, V.; Sort, J.; Stoyanov, S.; Givord, D. *Phys. Rev. Lett.* **2006**, *97*, 157203.

(18) Masala, O.; Seshadri, R. *J. Am. Chem. Soc.* **2005**, *127*, 9354–9355.

(19) Seo, W. S.; Jo, H. H.; Lee, K.; Kim, B.; Oh, S. J.; Park, J. T. *Angew. Chem., Int. Ed.* **2004**, *43*, 1115–1117.

(20) Riveiro, J. M.; De Toro, J. A.; Andrés, J. P.; González, J. A.; Muñoz, T.; Goff, J. P. *Appl. Phys. Lett.* **2005**, *86*, 172503.

(21) Morel, R.; Brenac, A.; Portemont, C. *J. Appl. Phys.* **2004**, *95*, 3757–3760.

(22) Dobrynin, A. N.; Ievlev, D. N.; Temst, K.; Lievens, P.; Margueritat, J.; Gonzalo, J.; Afonso, C. N.; Zhou, C. Q.; Vantomme, A.; Piscopiello, E.; Van Tendeloo, G. *Appl. Phys. Lett.* **2005**, *87*, 012501.

(23) Del Bianco, L.; Fiorani, D.; Testa, A. M.; Bonetti, E.; Savini, L.; Signoretti, L. *Phys. Rev. B* **2002**, *66*, 174418.

(24) Si, P. Z.; Li, D.; Choi, C. J.; Li, Y. B.; Geng, D. Y.; Zhang, Z. D. *Solid State Commun.* **2007**, *142*, 723–726.

(25) Johnston-Peck, A. C.; Wang, J. W.; Tracy, J. B. *ACS Nano* **2009**, *3*, 1077–1084.

(26) Zhou, S. M.; Imhoff, D.; Yu-Zhang, K.; Leprince-Wang, Y. *Appl. Phys. A: Mater. Sci. Process.* **2005**, *85*, 115–118.

(27) Tracy, J. B.; Weiss, D. N.; Dinega, D. P.; Bawendi, M. G. *Phys. Rev. B* **2005**, *72*, 064404.

(28) Luna, C.; Morales, M. D.; Serna, C. J.; Vazquez, M. *Nanotechnology* **2004**, *15*, S293–S297.

(29) Inderhees, S. E.; Borchers, J. A.; Green, K. S.; Kim, M. S.; Sun, S.; Strycker, G. L.; Aronson, M. S. *Phys. Rev. Lett.* **2008**, *101*, 117202.

(30) Gangopadhyay, S.; Hadjipanayis, G. C.; Sorensen, C. M.; Klabunde, K. J. *IEEE Trans. Magn.* **1993**, *29*, 2602–2607.

(31) Zeng, H.; Li, J.; Wang, Z. L.; Liu, J. P.; Sun, S. H. *Nano Lett.* **2004**, *4*, 187–190.

(32) Lu, B.; Huang, H.; Dong, X. L.; Zhang, X. F.; Lei, J. O.; Sun, J. P.; Dong, C. *J. Appl. Phys.* **2008**, *104*, 114313.

(33) Habib, A. B.; Ondeck, C. L.; Chaudhary, P.; Bockstaller, M. R.; McHenry, M. E. *J. Appl. Phys.* **2008**, *103*, 07A307.

(34) Salazar-Alvarez, G.; Sort, J.; Suriñach, S.; Baró, M. D.; Nogués, J. *J. Am. Chem. Soc.* **2007**, *129*, 9102–9108.

(35) Golosovsky, I. V.; Salazar-Alvarez, G.; López-Ortega, A.; González, M. A.; Sort, J.; Estrader, M.; Suriñach, S.; Baró, M. D.; Nogués, J. *Phys. Rev. Lett.* **2009**, *102*, 247201.

(36) Berkowitz, A. E.; Rodriguez, G. F.; Hong, J. I.; An, K.; Hyeon, T.; Agarwal, N.; Smith, D. J.; Fullerton, E. E. *Phys. Rev. B* **2008**, *77*, 024403.

(37) Berkowitz, A. E.; Rodriguez, G. F.; Hong, J. I.; An, K.; Hyeon, T.; Agarwal, N.; Smith, D. J.; Fullerton, E. E. *J. Phys. D* **2008**, *41*, 134007.

(38) Djerdj, I.; Ačcon, D.; Jagličić, Z.; Niederberger, M. *J. Phys. Chem. C* **2007**, *111*, 3614–3623.

(39) Wang, Z. H.; Geng, D. Y.; Hu, W. J.; Ren, W. J.; Zhang, Z. D. *J. Appl. Phys.* **2009**, *105*, 07A315.

(40) Si, P. Z.; Li, D.; Lee, J. W.; Choi, C. J.; Zhang, Z. D.; Geng, D. Y. U. *Appl. Phys. Lett.* **2005**, *87*, 133122.

(41) Zhou, S. M.; Shi, L.; Yang, H. P.; Wang, Y.; He, L. F.; Zhao, J. Y. *Appl. Phys. Lett.* **2008**, *93*, 182509.

(42) Markovich, V.; Fita, I.; Wisniewski, A.; Puzniak, R.; Mogilyansky, D.; Titelman, L.; Vradman, L.; Herskowitz, M.; Gorodetsky, G. *Phys. Rev. B* **2008**, *77*, 054410.

(43) Kavich, D. W.; Dickerson, J. H.; Mahajan, S. V.; Hasan, S. A.; Park, J. H. *Phys. Rev. B* **2008**, *78*, 174414.

(44) Shin, J. M.; Anisur, R. M.; Ko, M. K.; Im, G. H.; Lee, J. H.; Lee, I. S. *Angew. Chem., Int. Ed.* **2009**, *48*, 321–324.

(45) An, K.; Kwon, S. G.; Park, M.; Na, H. B.; Baik, S. I.; Yu, J. H.; Kim, D.; Son, J. S.; Kim, Y. W.; Song, I. C.; Moon, W. K.; Park, H. M.; Hyeon, T. *Nano Lett.* **2008**, *8*, 4252–4258.

(46) Yun, B. K.; Koo, Y. S.; Jung, J. H. *J. Magn.* **2009**, *14*, 147–149.

(47) Hansen, T. C.; Henry, P. F.; Fischer, H. E.; Torregrossa, J.; Convert, P. *Meas. Sci. Technol.* **2008**, *19*, 034001.

(48) Rodriguez-Carvajal, J. *Phys. B* **1993**, *192*, 55–69. (http://www.ill.eu/sites/fullprof).

Table 1. Summary of the Synthesis Conditions and the Structural Parameters Obtained from Neutron Diffraction and TEM Analyses

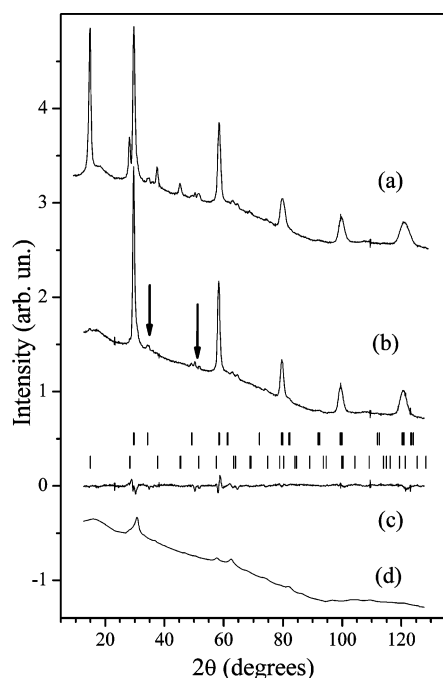|	synthesis params				neutron analysis				TEM		
sample	[S]:[M] (mol/mol)	[Mn^{2+}] (mol/mL)	T (°C)	t (min)	D_{MnO} (nm)	a_{MnO} (Å)	D_{shell} (nm)	t_{shell} (nm)	D_{tot} (nm)	D_{MnO} (nm)	t_{shell} (nm)
M1	1.03	0.05	240	30	19(2)	4.4200(8)	2.8(3)	1.5	25(6)	21	4−5
M2	41.3	0.03	205	60	17.0(5)	4.4424(2)	5.0(2)	0.15	15(5)	14	2−3
M3	4.1	0.05	220	30	15.7(5)	4.4431(6)	5.0(2)	0.5	13(5)	10	3−4
M4	20	0.04	190	30	4.7(3)	4.374(2)	4.9(3)	2	5(1)	3	2−3

Figure 1. Neutron diffraction patterns measured at (a) 20 K and (b) 250 K for sample M2. The small reflections shown by the arrows are due to the cryostat and the sample holder. (c) Difference pattern (calculated − observed) at 250 K. (d) Calculated pattern from the shell γ-Mn_2O_3−Mn_3O_4, showing its contribution to the total patterns (a) and (b). The stripes mark the positions of the Bragg reflections from the MnO core: upper and lower rows correspond to the magnetic and nuclear reflections, respectively.
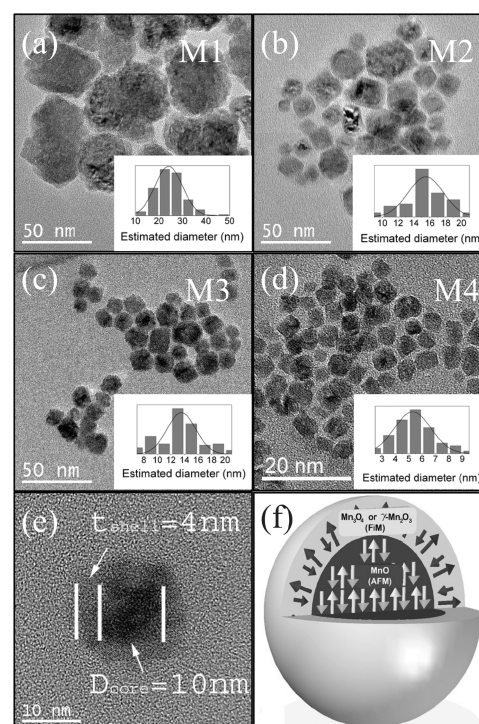

Figure 2. Transmission electron micrographs of samples (a) M1, (b) M2, (c) M3 and (d) M4 (note the different magnification). Shown in the respective insets are the corresponding particle size distributions with a fit to a log-norm function. (e) High-resolution image of an M2 nanoparticle. (f) Schematic representation of the morphological and magnetic structures of the nanoparticles.

2010F instrument with a field-emission gun operating at 200 kV, the latter equipped with a postcolumn Gatan Image Filter (GIF) energy spectrometer. The particle size, D_{MnO}, and its standard deviation were obtained by calculating the number average by manually measuring the equivalent diameters of >200 particles from TEM micrographs (Figure 2).

Electron energy loss spectra (EELS) were acquired at about every 0.5 nm along the diameter of the nanoparticles (as schematically shown in Figure 3a) at an energy range containing the Mn-$L_{2,3}$ and the O-K edges, with an energy resolution of 0.8 eV (see Figure 3b). Mn/O quantification was carried out using Gatan Digital Micrograph commercial software. The Mn oxidation state was obtained from the Mn-L_3 peak onset and L_3/L_2 intensity ratios[49,50] using the homemade software package MANGANITAS.[51−53] The L_3/L_2 intensity ratio for all samples is subject to a relative error of about 5% except for sample M1, where the nanoparticles are exceedingly large, leading to a weaker EELS signal and consequently to larger errors. Note that several particles were measured for each sample.

dc magnetic measurements were carried out on loosely packed powdered samples using a superconducting quantum interference device (SQUID, Quantum Design) magnetometer with 70 kOe maximum field. The magnetization measurements were carried out at 50 Oe. The hysteresis loops were measured at $T = 10$ K after field cooling in $H_{FC} = 20$ kOe from $T = 200$ K.

The ac susceptibility measurements were performed at different frequencies, between 10 Hz and 10 kHz, applying an ac field of 10 Oe using physical properties measurement system (PPMS, Quantum Design) equipment.

The temperature dependence of the electron spin resonance (ESR) spectra were recorded by a Bruker ESP300 spectrometer at 9.5 GHz. The parameters that characterize the resonance signal are the resonance field H_r, the line width ΔH, and the spectrum intensity, I_{ESR}. From the H_r value, at room temperature, we derived the gyromagnetic factor g through the resonance condition $h\nu = g\mu_B H_r$, where h and μ_B are Planck's constant and Bohr magneton, respectively. The line width is a measurement of the spin-relaxation mechanism, and it is measured as the distance between the peaks in the derivative of the absorption spectrum. The spectrum intensity

(49) Kurata, H.; Colliex, C. *Phys. Rev. B* **1993**, *48*, 2102–2108.

(50) Egerton, R. F. *Electron Energy-Loss Spectroscopy in the Electron Microscope*, 2nd ed.; Kluwer: Dordrecht, The Netherlands, 1996.

(51) Estradé, S.; Arbiol, J.; Peiró, F.; Abad, Ll.; Laukhin, V.; Balcells, Ll.; Martı́nez, B. *Appl. Phys. Lett.* **2007**, *91*, 252503.

(52) Estradé, S.; Arbiol, J.; Peiró, F.; Infante, I. C.; Sánchez, F.; Fontcuberta, J.; de la Peña, F.; Walls, M.; Colliex, C. *Appl. Phys. Lett.* **2008**, *93*, 112505.

(53) Estradé, S.; Rebled, J. M.; Arbiol, J.; Peiró, F.; Infante, I. C.; Herranz, G.; Sánchez, F.; Fontcuberta, J.; Córdoba, R.; Mendis, B. G.; Bleloch, A. L. *Appl. Phys. Lett.* **2009**, *95*, 072507.

(54) Schmid, H. K.; Mader, W. *Micron* **2006**, *37*, 426–432.

ARTICLES
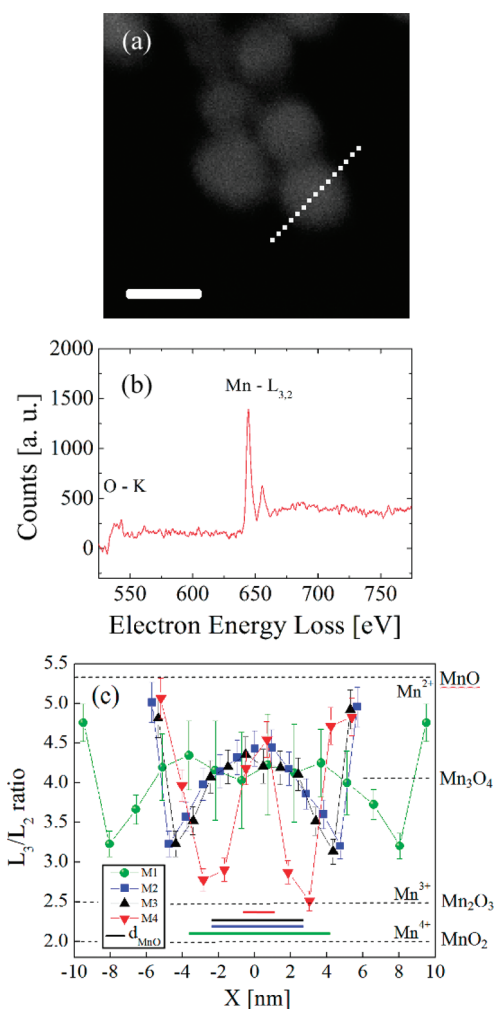*López-Ortega et al.*

Figure 3. (a) High-angle annular dark field (HAADF) image of M4 nanoparticles, where the approximate positions at which spectra were taken are indicated by dots. (b) Typical background-subtracted EEL spectrum of the shell part for M4. (c) Mn-L_3/L_2 intensity ratio along the diameter of the M1−M4 nanoparticles. The lines joining the data points are guides to the eye. The dotted lines in the figure are the expected L_3/L_2 ratios for Mn^{2+}, Mn^{3+}, and Mn^{4+} ions, respectively.[49,54] The thick solid lines in (c) indicate the diameter of the core as estimated from the position dependence of the Mn-L_3/L_2 intensity ratio.

is the area under the absorption curve and is proportional to the concentration of resonant magnetic ions.

Results and Discussion

Structural and Morphological Characterization. As can be seen from the high-temperature neutron diffraction (shown in curve b in Figure 1 and Figure S1 for samples M2 and M4, respectively), the MnO core exhibits the expected rock salt crystal structure. However, although samples M1−M3 show a stoichiometric structure, sample M4 has defects on the Mn sites with a 0.74(2) occupancy ratio.[35] Concerning the shell structure sample, M4 does not exhibit the expected hausmannite, Mn_3O_4, structure[34,36,37] but a spinel type tetragonal γ-Mn_2O_3 structure.[35,56] For samples M1−M3 the neutron diffraction signal is overwhelmed by the MnO spectrum (see curve d in Figure 1); thus, it is impossible to distinguish between the γ-Mn_2O_3 and the Mn_3O_4 structures for the shell.

All the studied samples show a similar temperature dependence of the lattice parameter for MnO, which displays a distinct feature around 125 K: i.e., at the MnO Néel temperature.[35] This is similar to the behavior observed in the bulk,[57] implying a rather well structured MnO core. Interestingly, the lattice parameter of MnO is contracted with respect to the bulk and becomes smaller as the core size decreases (see Table 1), in contrast with most oxide nanoparticle systems which show a lattice expansion for reduced particle sizes.[58] The smaller lattice parameter is likely caused by the presence of a large number of defects, since no stresses due to the outer passivation layer were detected. In most of the samples the contribution from the MnO core dominates in the diffraction patterns; therefore, the lattice parameters of the shell were determined with lower accuracy. We did not observe any essential difference in the temperature dependence of the lattice parameters of the different samples, which were evaluated as $a = 5.844(5)$ Å and $c = 9.13(1)$ Å.

From the fitting of the different patterns at diverse temperatures the structural and magnetic characteristic sizes and structures can be readily obtained. The diffraction peak broadening comprises two contributions, which have different q dependencies: internal stresses (i.e., microstrains) and crystallite size effect. The profile analysis of the diffraction patterns shows that the stresses are negligible within experimental error. Therefore, from the peak broadening one can easily obtain the volume-averaged crystallite size and the magnetic domain size.

The volume-averaged diameter of the MnO core, D_{MnO}, and the characteristic sizes of ferrimagnetic nanoparticles forming the shell, D_{shell}, are shown in Table 1. Interestingly, while D_{MnO} ranges from 5 to 19 nm on adjusting the synthesis conditions, D_{shell} remains rather constant at around 3−5 nm. Note that due to the limited statistics it is not possible to directly evaluate any anisotropy in the particle shape, from the peak profile analysis. However, from the core/shell volume ratios obtained from the fit, indirect information can be inferred. Taking into account the volume ratios and the measured diameters of the cores and assuming a uniform core/shell structure, the corresponding averaged effective thickness of the shell, t_{shell}, can be estimated (see Table 1). Hence, on comparison of the effective shell thickness and the shell crystallite sizes obtained from the profile refinement it can be concluded that the nanoparticles forming the ferrimagnetic shell layer are strongly anisotropic (e.g., pancakelike).

In order to confirm this feature, TEM images of the samples were obtained, and the results are summarized in Table 1. All the samples exhibit a clear core/shell structure with average overall particle sizes, D_{tot}, of 25(6) nm for M1, 15(5) nm for M2, 13(5) nm for M3, and 5(1) nm for M4 (where the value in parentheses is the log-norm standard deviation; see insets in Figure 2). The shell thicknesses, t_{shell}, remain rather homogeneous, in the range of ∼2−5 nm (see Table 1). Note that the shells are more difficult to image, since each individual particle needs a specific imaging tilt to allow the shell to be clearly observed (see Figure 2e). Thus, the statistics are not sufficient to evaluate standard deviations and only estimates are given. The values of the core diameter obtained from TEM and neutron diffraction follow a similar trend, where the small discrepancies probably arise from the different averaging methods (number

(56) Goodenough, J. B.; Loeb, A. L. *Phys. Rev.* **1955**, *98*, 391–408.

(57) Morosin, B. *Phys. Rev. B* **1970**, *1*, 236–243.
(58) Zheng, X. G.; Kubozono, H.; Yamada, H.; Kato, K.; Ishiwata, Y.; Xu, C. N. *Nat. Nanotechnol.* **2008**, *3*, 724–726.

average vs volume average).[59,60] As for the shell thicknesses, the TEM values follow a trend similar to the effective thickness.

To further evaluate the structure of the particles, a detailed EELS study was carried out by indirectly evaluating the Mn oxidation state from the Mn/O ratio, the Mn-L_3 onset, and the Mn-L_3/L_2 intensity ratios. Importantly, data obtained for different particles belonging to the same sample showed no relevant differences. The dependence of the Mn-L_3/L_2 ratio on the position for the four samples, M1–M4, is given in Figure 3c. For all the analyzed nanoparticles an MnO core is observed and its radius increases from M4 to M1 (see the solid lines at the bottom of Figure 3c), in agreement with TEM and neutron diffraction analyses shown in Table 1. Note that when an EELS signal is obtained from the center of a nanoparticle, the signal arises from both the core and the enveloping shell, making it thereby impossible to obtain the Mn-L_3/L_2 values reported in the literature for MnO.[49,54] However, a quantitative simulation taking into account the core–shell structure confirms the MnO character of the core. Concerning the shell part, the L_3/L_2 values for M4 almost reach those corresponding to a Mn^{3+} oxidation state indicating a Mn_2O_3 structure, in agreement with the neutron diffraction results. A noticeable increase of the L_3/L_2 values toward the value for a Mn^{2+} oxidation state can be observed for the rest of the samples, thus indicating the presence of Mn_3O_4 in the shell for the larger particles (M1–M3). Additionally, a very thin (less than 1 nm) MnO superficial layer was observed in all the studied particles. The origin of this effect is unclear. It could be attributed to either an artifact resulting from the reduction of some outer Mn^{3+} ions to Mn^{2+} by the electron beam,[55] although it is not possible to rule out an increase of the reducing power of the surfactant due to some external parameters (e.g., electron or neutron beams).

Magnetic Properties. From the low-temperature neutron diffraction pattern (curve a in Figure 1 and Figure S1 for M2 and M4, respectively) it is found that for all samples the MnO cores exhibit the expected AFM structure observed in the bulk.[61] However, for sample M4, the γ-Mn_2O_3 shell has a simple Néel type FiM structure[35] rather than the more complex structure observed in Mn_3O_4 (see Figure S2b in the Supporting Information).[62] For samples M1–M3, due to the large MnO scattering caused by the large core/shell volume ratio, no magnetic signal from the shell can be detected within the limits of our accuracy (about 0.5 μ_B) (see Figure S2a).

Remarkably, T_N of the nanoparticles appears to be higher than that in the bulk and increases for smaller MnO cores. To further confirm this T_N enhancement, the temperature dependence of the neutron diffraction pattern was analyzed in detail. In Figure 4a the magnetic moment derived from the temperature dependence of the integral intensity of the $(^1/_2, ^1/_2, ^1/_2)$ magnetic reflection of MnO is shown for sample M2. The value of the magnetic moment in saturation was defined from the profile analysis of the pattern measured at 10 K. In this calculation we used the known magnetic order for MnO, observed in the bulk
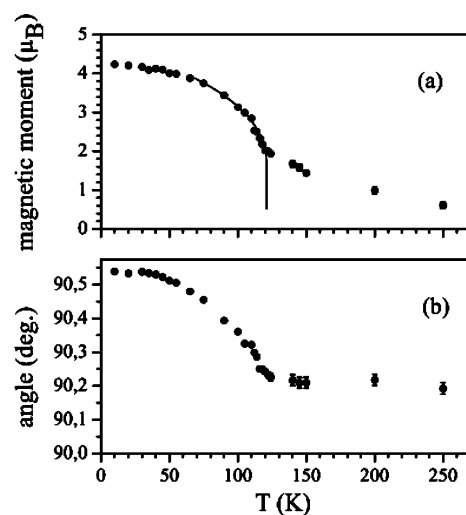

Figure 4. (a) Temperature dependence of the magnetic moment/ion in the MnO core for sample M2. The solid lines correspond to a fit with a power law. (b) Temperature dependence of the angle of trigonal distortion.

Table 2. Summary of the Effective Néel Temperature and Sublattice Magnetization for the MnO Core, M_{MnO}

sample	T_N (K)	M_{MnO} (μ_B)
M1	123(1)	4.25(7)
M2	120.9(2)	4.21(2)
M3	126.0(2)	3.83(8)
M4	139(10)	4.3(5)

as well as in "restricted geometry",[63,64] taking into account the trigonal distortion due to magnetostriction[65] shown in Figure 4b. As expected, the value of the saturated magnetic moment appears smaller than the 5 μ_B for the free Mn^{2+} ion (see Table 2). This is a known effect and is readily explained by the spin disordering at the core surface (i.e., at the interface in our case),[63] although some spin canting in the core[66] or partial oxidation of the Mn ions cannot be ruled out. Assuming the temperature dependence of the magnetic moment follows a power law in the temperature range of the main drop of magnetic moment (note the "tail" in m for higher temperatures), the effective Néel temperature of the MnO cores was evaluated as 120.9(2) K for M2 (Figure 4a). Similar analyses for the other samples lead to T_N = 120.9(2)–139(10) for M1–M4 (see Figure 5 and Table 2). Note that a T_N enhancement has been also observed in MnO confined in different porous templates[63,64] (see Figure 5) and in other manganese oxides,[67,68] although it is not present in MnF_2 films.[69] The origin of this effect has been proposed to arise from size and surface effects, where the broken symmetry at the surface and the concomitant local disorder may lead to (i) enhancement of the exchange interaction between surface

(59) Allen, T. *Particle Size Measurements*, 5th ed.; Chapman & Hall: London, 1997.

(60) Chen, D. X.; Sanchez, A.; Taboada, E.; Roig, A.; Sun, N.; Gu, H. C. *J. Appl. Phys.* **2009**, *105*, 083924.

(55) Pan, Y.; Sader, K.; Powell, J. J.; Bleloch, A.; Gass, M.; Trinick, J.; Warley, A.; Brydson, A. L.; Brown, A. *J. Struct. Biol.* **2009**, *166*, 22–31.

(61) Roth, W. L. *Phys. Rev.* **1958**, *110*, 1333–1341.

(62) Jensen, G. B.; Nielsen, O. V. *J. Phys. C* **1974**, *7*, 409–424.

(63) Golosovsky, I. V.; Mirebeau, I.; André, G.; Kurdyukov, D. A.; Kumzerov, Y. A.; Vakhrushev, S. B. *Phys. Rev. Lett.* **2001**, *86*, 5783–1786.

(64) Golosovsky, I. V.; Mirebeau, I.; Sakhnenko, V. P.; Kurdyukov, D. A.; Kumzerov, Y. A. *Phys. Rev. B* **2005**, *72*, 144409.

(65) Lines, M. E.; Jones, E. D. *Phys. Rev.* **1965**, *113*, A1313.

(66) Theil Kuhn, L.; Bojesen, A.; Timmermann, L.; Meedom Nielsen, M.; Mørup, S. *J. Phys.: Condens. Matter* **2002**, *14*, 13551–13567.

(67) Tang, Z. X.; Sorensen, C. M.; Klabunde, K. J.; Hadjipanayis, G. C. *Phys. Rev. Lett.* **1991**, *67*, 3602–3605.

(68) Yang, A.; Chinnasamy, C. N.; Greneche, J. M.; Chen, Y. J.; Yoon, S. D.; Chen, Z. H.; Hsu, K. L.; Cai, Z. H.; Ziemer, K.; Vittoria, C.; Harris, V. G. *Nanotechnology* **2009**, *20*, 185704.

(69) Golosovsky, I. V.; Sokolov, N. S.; Gukasov, A.; Bataille, A.; Boehm, M.; Nogués, J. *J. Magn. Magn. Mater.* **2010**, *322*, 664–667.
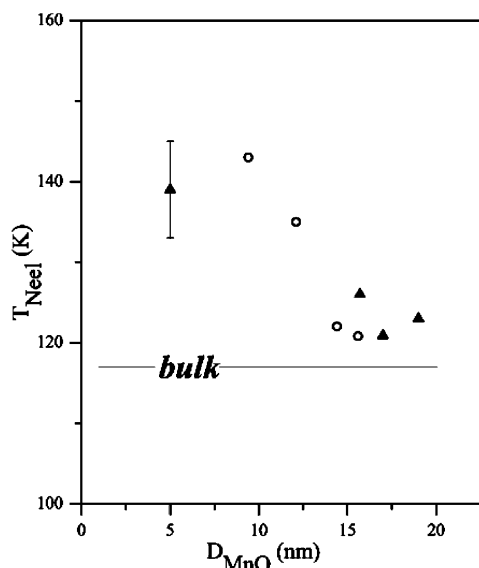
ohio2/yja-yja/yja-yja/yja99907/yja4389d07z | xppws | 23:ver.3 | 6/11/10 | 10:07 | Msc: ja-2010-021798 | TEID: mjw00 | BATID: 00000

A R T I C L E S
López-Ortega et al.

Figure 5. Dependence of the Néel temperature, effective T_N, for the MnO cores in the core/shell nanoparticles (triangles) and MnO nanoparticles embedded within porous glass (circles)[73] on the core size D_{MnO}.

Figure 6. (a) Temperature dependence of the fwhm of the MnO ($^1/_2$, $^1/_2$, $^1/_2$) magnetic reflection for sample M2. (b) Size (averaged diameter) of the magnetic domain deduced from the peak broadening.

atoms with respect to bulk exchange interactions[70] and (ii) variations in the crystal field resulting in high-spin−low-spin transitions[71] and/or the appearance of new degrees of freedom which interact with the AFM order parameter.[64] Moreover, other effects such as the observed size dependence of the lattice parameter may also play a role.[72]

Remarkably, as can be seen in Figure 4a for sample M2, with a thin passivation shell, the observed antiferromagnetic order in MnO does not vanish at the Néel temperature and persists up to room temperature, where the sublattice magnetization of MnO exhibits a "tail" up to high temperatures rather than vanishing above T_N.

Interestingly, the averaged diameter of the magnetic domains in the MnO core calculated from the broadening of the antiferromagnetic peak appears to be significantly smaller than the core diameter: −6.7(5) vs 17.0(5) nm (M2) and 9(1) vs 19(2) nm (M1). Note that due to peak overlapping the magnetic size could only be determined for samples M1 and M2. Similar domain size effects were observed in MnO nanoparticles embedded within different porous media.[63,64] In Figure 6 the temperature dependence of the full width at half-maximum (fwhm) of the MnO ($^1/_2$, $^1/_2$, $^1/_2$) magnetic reflection and volume average domain diameter are shown for M2. It is seen that the diameter drastically changes with temperature, reaching a minimum at temperatures well above T_N = 120.9 K. The results resemble a fragmentation of the magnetic domains observed in first-order transitions. However, due to size effects there should be a continuous magnetic transition,[74,75] in contrast to the bulk first-order transition.[61] In fact, the magnetic domain fragmentation may explain the large "tail" in the temperature dependence
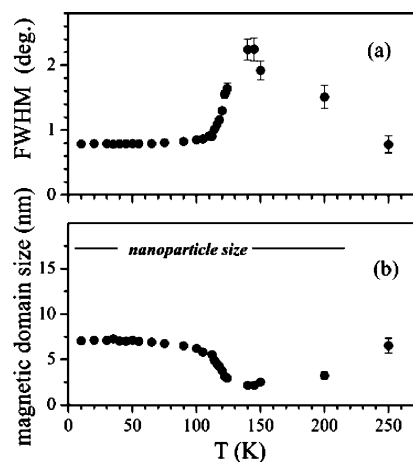
of the magnetic moment (Figure 4a), since smaller MnO entities have larger T_N values. Although some of these effects could be partially explained by the concomitant particle size distribution, they are exceedingly large to arise solely from this effect.

Shown in Figure 7 are the hysteresis loops of the samples at 10 K after field cooling in 20 kOe from 200 K. The saturation magnetization, M_S (obtained by using the total mass), is different for each sample. Using the TEM values for the particle size and the shell thickness and assuming that the MnO core does not contribute to M_S, we can estimate the saturation magnetization of the shell. Despite the crude approximations the M_S values are rather consistent with $M_S \approx 32.0-37.7$ emu/g for M1−M3 and are slightly smaller for M4, $M_S \approx 27$ emu/g. These results are consistent with saturation magnetization for bulk Mn_3O_4 ($M_S \approx 38$ emu/g)[76] and γ-Mn_2O_3 nanoparticles ($M_S \approx 28$ emu/g).[77]

All the loops exhibit a large coercivity, H_C (see Figure 7), which is consistent with the rather large anisotropy of the γ-Mn_2O_3 or Mn_3O_4 phases.[77−80] Moreover, the coercivity is influenced by the coupling to the AFM core,[6] where the smallest core gives rise to the largest coercivity, in agreement with previous reports.[34] Moreover, as expected,[34,36,37] all the samples exhibit a loop shift along the field axis (exchange bias, H_E), evidencing the exchange coupling between the AFM core and the FiM shell.[6] The nonmonotonic dependence of H_E with the MnO core size (see Figure 7) is consistent with earlier results in the same system,[34] characterized by its inverse, $T_N > T_C$, magnetic structure.[81,82]

The temperature dependence of the FC and ZFC magnetization measured with H = 50 Oe (Figure 8) reveals that all the samples exhibit their main magnetic features below $T \approx 50$ K, consistent with the known Curie temperature, T_C = 39 and 42 K, of the γ-Mn_2O_3 and Mn_3O_4 phases, respectively.[77,80,84] Thus, the magnetization is largely dominated by the ferrimagnetic

(70) Wesselinowa, J. M. *J. Magn. Magn. Mater.* **2010**, *322*, 234–237.
(71) Morales, M. A.; Skomski, R.; Fritz, S.; Shelburne, G.; Shiled, J. E.; Yin, M.; O'Brien, S.; Leslie-Pelecky, D. L. *Phys. Rev. B* **2007**, *75*, 134423.
(72) Kantor, I.; Dubrovinsky, L.; McCammon, C.; Dubrovinskaia, L.; Goncharenko, I.; Kantor, A.; Kuznetsov, A.; Crichton, W. *Phase Trans.* **2007**, *80*, 1151–1167.
(73) Golosovsky, I. V. Private communication.
(74) Imry, Y. *Phys. Rev. B* **1980**, *21*, 2042–2043.
(75) Challa, M. S. S.; Landau, D. P.; Binder, K. *Phys. Rev. B* **1986**, *34*, 1841–1852.

(76) Jacobs, I. S. *J. Phys. Chem. Solids* **1959**, *11*, 1–11.
(77) Kim, S. H.; Choi, B. J.; Lee, G. H.; Oh, S. J.; Kim, B.; Choi, H. C.; Park, J.; Chang, Y. *J. Korean Phys. Soc.* **2005**, *46*, 941–944.
(78) Dwight, K.; Menyuk, N. *Phys. Rev.* **1960**, *119*, 1470–1479.
(79) Du, C. S.; Yun, J. D.; Dumas, R. K.; Yuan, X. Y.; Liu, K.; Browning, N. D.; Pan, N. *Acta Mater.* **2008**, *56*, 3516–3522.
(80) Tackett, R.; Lawes, G.; Melot, B. C.; Grossman, M.; Toberer, E. S.; Seshadri, R. *Phys. Rev. B* **2007**, *76*, 024409.
(81) Cai, J. W.; Liu, K.; Chien, C. L. *Phys. Rev. B* **1999**, *60*, 72–75.
(82) Nogués, J.; Schuller, I. K. *J. Magn. Magn. Mater.* **1999**, *192*, 203–232.
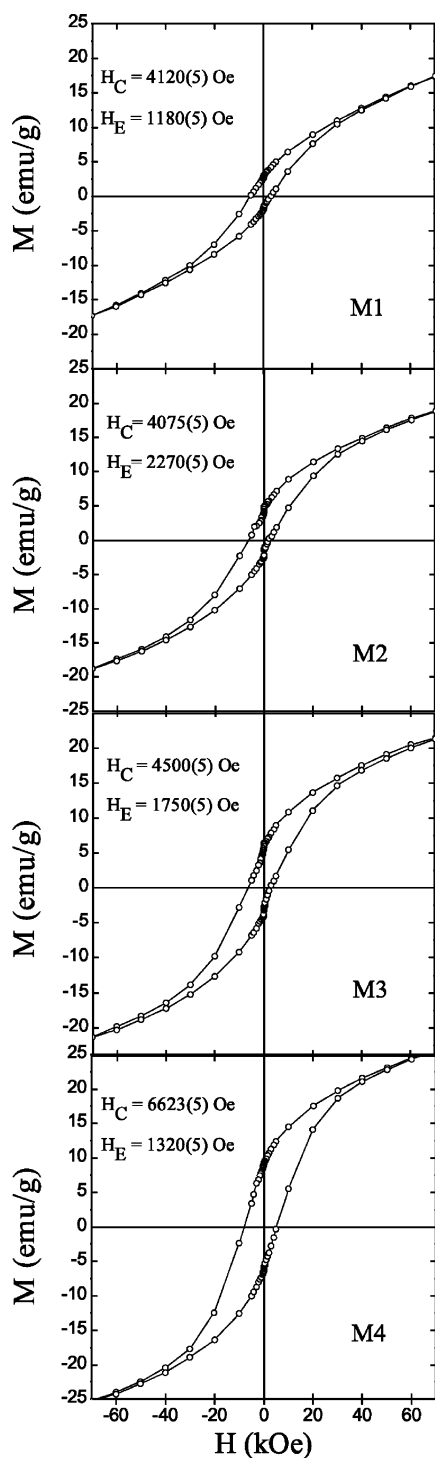(84) Srinivasan, G.; Seehra, M. S. *Phys. Rev. B* **1983**, *28*, 1–7.

Figure 7. Hysteresis loops for samples M1−M4 at $T = 10$ K after field cooling from $T = 200$ K in $H_{FC} = 20$ kOe. The values of H_E and H_C are indicated in the respective panels.
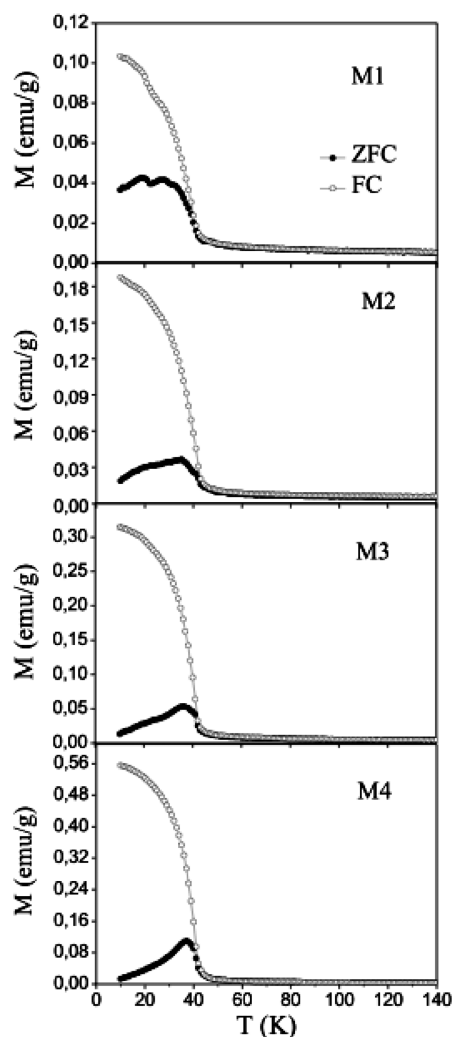

Figure 8. Temperature dependence of the field cooled (FC) and zero field cooled (ZFC) magnetizations for samples M1−M4 measured in $H = 50$ Oe.

counterpart. Interestingly, it can be seen that the ZFC branch of samples M1−M3 exhibits fine structure below $T_C \approx 42$ K and there is a hump at $T \approx 33$ K and a second anomaly at $T \approx 20$ K. In contrast, for sample M4 both the FC and ZFC curves are featureless.

To gain further insight into the nature of the low-temperature anomalies, ac susceptibility measurements were carried out. Figure 9 shows the real (χ') and imaginary (χ'') components of the ac susceptibility measured at different frequencies from 10 Hz to 10 kHz on applying an ac field of 10 Oe. The larger

nanoparticles present anomalies in χ' and χ'' at 41, 36, and 20 K. These anomalies are frequency independent, implying that they are thermodynamic transitions rather than blocking temperatures. The transition temperatures are consistent with the reported $T_C = 42$ K and the reorientation transitions of Mn_3O_4 ($T_{RO} = 39$ K and $T_{RO}* = 33$ K).[62] For M4, instead, the ac susceptibility exhibits a single transition, as was also observed in the $M(T)$ dc magnetization curve. This result is not consistent with the magnetic behavior of the Mn_3O_4 phase, in agreement with neutron diffraction and EELS results which indicate that the M4 shell is solely formed by γ-Mn_2O_3. The experimental results suggest the following picture for the systems: the nanoparticles present a core/shell structure with AFM MnO core and a FiM shell that changes its composition (γ-Mn_2O_3 and/or Mn_3O_4) depending on the nanoparticle size, as shown schematically in Figure 2f.

Electron Spin Resonance. In order to quantify the core/shell composition, we also performed an ESR spectroscopy study. Figure 10 shows representative ESR spectra for temperatures above and below T_N for M1−M4. Above T_N the spectra exhibit two resonance lines, one narrow and one broad, both centered at around $H_r = 3370$ Oe. This corresponds to a gyromagnetic factor of $g \approx 2.00$, which is consistent with the values reported
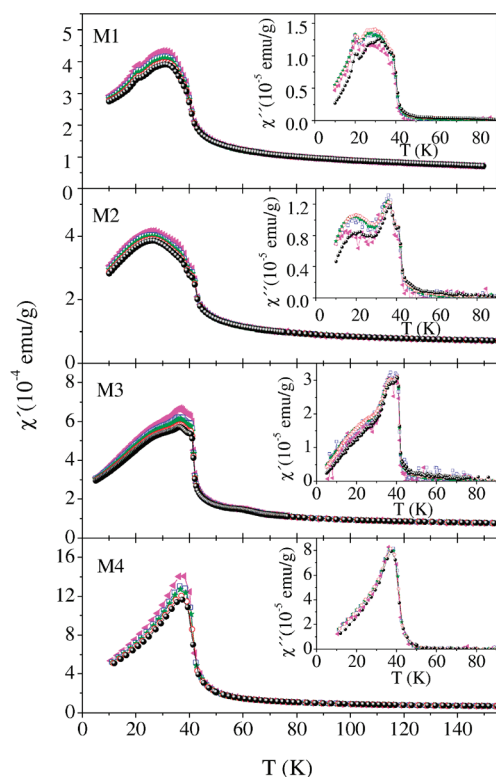
ohio2/yja-yja/yja-yja/yja99907/yja4389d07z | xppws | 23:ver.3 | 6/11/10 | 10:07 | Msc: ja-2010-021798 | TEID: mjw00 | BATID: 00000

A R T I C L E S   *López-Ortega et al.*

Figure 9. Temperature dependence of in-phase (χ') and out-of-phase (χ'') ac susceptibilities for samples M1−M4 measured at different frequencies: (▲) 80 Hz; (□) 600 Hz; (★) 1250 Hz; (○) 5000 Hz; (●) 10 000 Hz.
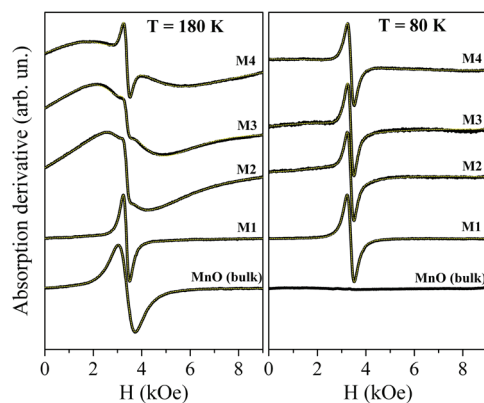

Figure 10. ESR spectra for the four samples M1−M4 and bulk MnO above and below T_N. The dotted line corresponds to the fitting curve (color on line). Note that for sample M1 the main ESR line corresponds to the shell resonance which remains below T_N.

402 in the literature ($g = 2.02−2.00$ for $Mn_3O_4^{[83-85]}$ and $g =$
403 $1.997−2.001$ for $MnO^{[86-88]}$). When the temperature decreases,
404 ΔH increases for the broad signal, and at $T \approx 120$ K it is no
405 longer detected. The narrow signal, instead, is observed in the
406 entire measured temperature range and presents a nonmonotonic
407 temperature evolution.

408 It is known that below the AFM transition temperature,
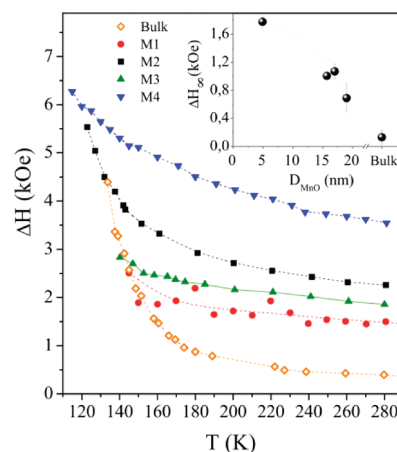409 because of the large anisotropy and exchange fields present,

Figure 11. Temperature dependence of the ESR line width, ΔH, corresponding to the MnO core phase for samples M1−M4. For comparison, the parameters corresponding to the MnO bulk phase are also included. The inset shows the evolution of ΔH_∞ with the MnO core size.

the spin equilibrium state changes and the AFM resonance 410
modes cannot be excited. Therefore, T_N is usually determined 411
by the disappearance of the ESR spectrum.[89] This behavior is 412
reproduced by the AFM MnO pure phase, as was reported by 413
several authors.[86-88] This fact allowed us to identify the broad 414
ESR resonance as coming from the AFM MnO (core) phase, 415
while the narrow line is assigned to the shell phase, as will be 416
explained later. 417

In order to quantify and extract reliable ESR parameters, we 418
fitted the total spectral signal with two Lorentzian lines centered 419
at $g \approx 2$. Figure 10 shows the ESR spectra with the corre- 420
sponding fitting curve. For comparison the resonance signal of 421
the MnO bulk sample is also included. Observe that all the 422
samples present the same qualitative behavior: two resonance 423
lines for $T > T_N$, where the relative intensities are different for 424
each M1−M4 system, and a narrow resonance for $T < T_N$. Apart 425
from the main narrow resonance, below $T \approx 40$ K a second 426
broad low-field resonance was also observed in a small 427
temperature range. This line shifts toward zero field, and at T 428
≈ 27 K it is no longer detected. A low-field resonance with 429
identical temperature and field behavior is present in the Mn_3O_4 430
pure oxide.[84,85] This resonance is attributed to the FiM resonance 431
of ordered magnetic domains at different orientation respect to 432
the magnetic field.[84] 433

The temperature dependence of ΔH obtained from the fitting 434
curves for the core and the shell components are shown in 435
Figures 11 and 12a. The ESR parameters for bulk MnO (Figure 436 **F12**
11) and Mn_3O_4 (inset Figure 12a) are also included as reference. 437
From Figure 11 it is manifested that the line width of the MnO 438
core decreases when the size of the particle increases. At room 439
temperature $\Delta H \approx 3500$ Oe for M4 and approaches the bulk 440
value $\Delta H \approx 400$ Oe for larger sizes. The line width depends 441
on the magnetization relaxation mechanism. In the paramagnetic 442
range the following dependence was established: $\Delta H =$ 443
$C/(T\chi(T))\Delta H_\infty$,[86,90,91] where C is the Curie constant and ΔH_∞ 444
is the value reached by ΔH at high temperature. Assuming that 445
the susceptibility follows a Curie−Weiss dependence with a 446
Curie−Weiss temperature $\Theta \approx −600$ K, we have estimated 447

(83) Seehra, M. S.; Srinivasan, G. *J. Appl. Phys.* **1982**, *52*, 8345−8347.
(85) Winkler, E.; Zysler, R. D.; Fiorani, D. *Phys. Rev. B* **2004**, *70*, 174406.
(86) Dormann, E.; Jaccarino, V. *Phys. Lett.* **1974**, *48A*, 81−82.
(87) Ferrante, R. F.; Wilkerson, J. L.; Graham, W. R. M.; Weltne, W., Jr. *J. Chem. Phys.* **1977**, *67*, 5904−5913.
(88) Golosovsky, I. V.; Arcon, D.; Jaglicic, Z.; Cevc, P.; Sakhnenko, V. P.; Kurdyukov, D. A.; Kumzerov, Y. A. *Phys. Rev. B* **2005**, *72*, 144410.

(89) Huber, D. L.; Alejandro, G.; Caneiro, A.; Causa, M. T.; Prado, F.; Tovar, M.; Oseroff, S. B. *Phys. Rev. B* **1999**, *60*, 12155−12161.
(90) Causa, M. T.; et al. *Phys. Rev. B* **1998**, *58*, 3233−3239.
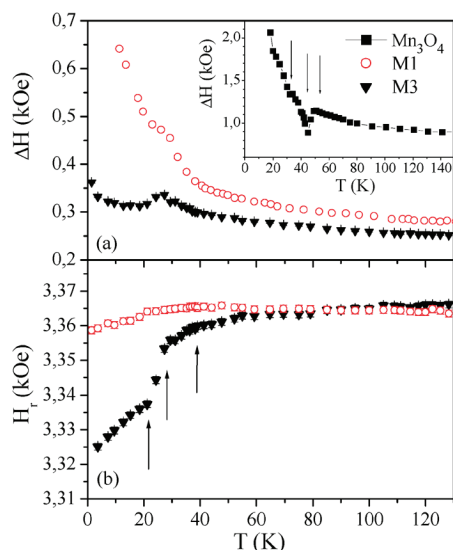(91) Huber, D. L. *J. Phys. Chem. Solids* **1971**, *32*, 2145−2149.

Figure 12. (a) Temperature dependence of the ESR line width, ΔH, corresponding to the Mn_3O_4 phase of the samples M1 and M3. For comparison, the measured parameters of the isolated Mn_3O_4 phase are also included in the inset. (b) Temperature dependence of the resonance field, H_r, for samples M1 and M3. The magnetic transitions are indicated by arrows.
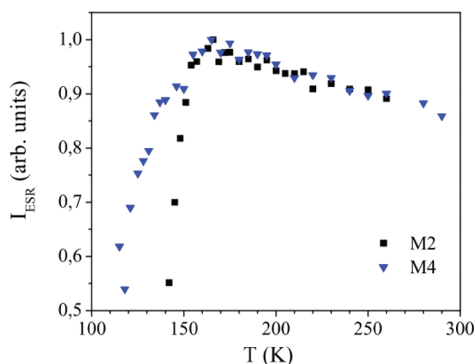

Figure 13. Temperature dependence of the ESR intensity of MnO, I_{ESR}, for samples M2 and M4.

ΔH_∞ as a function of the core particle size. From the inset of Figure 11 it is evident that ΔH_∞ increases, from the bulk value, by an order of magnitude when the size is reduced. The parameter ΔH_∞ is proportional to E_a^2/E_{ex}, where E_a and E_{ex} are the anisotropy and exchange interaction energies, respectively. When the particle size is reduced, E_{ex} should not be affected, in a first approximation, since it mainly originates from nearest neighbor interactions.[92] Therefore, the increase of ΔH_∞ implies a core magnetic anisotropy enhancement (by a factor of ∼3) when the size diminishes, as is observed for pure MnO nanoparticles,[71,88] probably related to surface or interface effects.[5,6,71] Note that the magnetization loops and the ESR experiment provide complementary information about the magnetic anisotropy; while in the first experiment the shell anisotropy is more significant, the ESR line width can sense the core anisotropy as a function of the size.

Figure 13 shows the temperature dependence of I_{ESR} for the MnO phase obtained from the fitting. As expected for an AFM compound, the ESR intensity decreases to zero at the ordering temperature. As can be observed, the AFM core transition is broad and the onset is located at $T \approx 150$ K. This result points out the presence of AFM short-range interaction well above the bulk T_N, in agreement with neutron diffraction results. Moreover, the broad I_{ESR} curve correlates with the tails in the MnO sublattice magnetization (and the domain fragmentation) observed by neutron diffraction.

In order to analyze the behavior of the shell-narrow ESR line, we show the ΔH temperature dependence of the Mn_3O_4 pure phase in the inset of Figure 12a, where several anomalies as a function of the temperature can be observed. These anomalies correspond to the FiM transition at $T_C = 42$ K and the spin reorientation transitions at 39 and 33 K.[84] These particular ΔH features are also reproduced by the narrow resonance signal observed in samples M1−M4, which enables us to identify this line as coming from the Mn_3O_4 phase. The temperature dependence of H_r also presents anomalies at similar temperatures. As can be observed in Figure 12b, H_r shifts toward lower values near T_C and shows anomalies at $T \approx 30$ and 20 K. These features are consistent with the results reported on Mn_3O_4,[84] hence corroborating that the low-temperature features found in the ac and dc susceptibility originate at the shell. The temperature dependence of the resonance field is explained by the presence of an effective anisotropy field (H_a) below T_C, which modifies the resonance condition $h\nu = g\mu_B(H_r + H_a)$.[93]

It is important to remark that the ground energy state of the Mn^{2+} ion corresponds to an orbital singlet $L = 0$; then the coupling with the lattice is very weak, and as a consequence the ESR line width is narrow and easily observed. On the other hand, the orbital degeneracy of the Mn^{3+} ion ground state ($3d^4$, $L = 2$) is not completely removed and presents important spin−orbit interaction; as a consequence Mn^{3+} usually does not show an ESR signal.[94] Therefore, it can be concluded that the narrow ESR line corresponds to the resonance of Mn^{2+} of the spinel Mn_3O_4, while the resonance of Mn^{3+} could not be detected. This conclusion is supported by several reported results on manganese oxides.[95,96] In these references, by thermal or chemical treatment, the valence of the manganese ions changes from Mn^{3+} to Mn^{2+}; as a consequence the ESR signal increases proportionally to the fraction of ions that are reduced from Mn^{3+} to Mn^{2+}. Moreover, this is also the reason why the γ-Mn_2O_3 phase, where all the manganese ions are Mn^{3+}, does not present a detectable ESR signal.

From the I_{ESR} values obtained from the fit for the narrow and broad signals (for $T \gg T_C, T_N$), the relative concentrations of Mn^{2+} ions of the MnO and Mn_3O_4 phases for each sample are calculated. The results are presented in Table 3. From this quantification it became evident that the overall concentration of the Mn_3O_4 diminishes when the nanoparticle size decreases. From the D_{tot} and D_{MnO} values obtained by TEM (Table 1) for M1−M4, we can estimate the Mn_3O_4 relative volume with respect to the total volume of the shell. These data are included in the last column of Table 3. These results indicate that the surface passivation of the MnO nanoparticles depends on the size of the particles. Larger particles tend to form Mn_3O_4 shells, while the smaller particles have γ-Mn_2O_3 shells consistent with

(92) Tobia, D.; Winkler, E.; Zysler, R. D.; Granada, M.; Troiani, H. E. *Phys. Rev. B* **2008**, *78*, 104412.

(93) Morrish, A. H., *The Physical Principles of Magnetism*; Wiley-IEEE Press: New York, 2001.

(94) Abragam, A.; Bleaney, B. *Electron Paramagnetic Resonance of Transition Ions*; Dover Publications: New York, 1986.

(95) Zhang, W.; Yang, Z.; Liu, Y.; Tang, S.; Han, X.; Chen, M. *J. Cryst. Growth* **2004**, *263*, 394–399.

(96) Kijlstra, W. S.; Poels, E. K.; Bliek, B. M.; Weckhuysen, B. M.; Schoonheydt, R. A. *J. Phys. Chem. B* **1997**, *101*, 309–316.

Table 3. Relative Concentration of Mn^{2+} in MnO and Mn_3O_4 Phase Obtained from the ESR Spectra[a]

sample	Mn^{2+} core	Mn^{2+} shell	$V_{Mn_3O_4}/V_{shell}$
M1	0.82(2)	0.18(2)	1
M2	0.985(3)	0.011(3)	0.1
M3	0.960(4)	0.032(3)	0.1
M4	0.995(1)	0.005(1)	0.005

[a] From D_{tot} and D_{MnO} obtained by TEM, the shell ratio $V_{Mn_3O_4}/V_{shell}$ is estimated and included in the last column.

neutron diffraction, EELS, and magnetic results. This fact can be understood from the Catlow and Fender model.[36,37,97] This model takes into account that the usual defects present in MnO are Mn vacancies, which are compensated by the oxidation of the manganese ion to Mn^{3+}. Therefore, the larger nanoparticles tend to form Mn_3O_4 at the surface. When the nanoparticle size is reduced, the density of defects increases, as was observed by neutron diffraction; consequently, γ-Mn_2O_3, where all the manganese ions are Mn^{3+}, will be the more stable shell phase.

Conclusions

In conclusion, we have studied the structural and magnetic properties of bimagnetic core/shell nanoparticles. We found that the nanoparticles present an AFM MnO core and an FiM surface shell. The shell composition depends on the nanoparticle size, the larger nanoparticles presenting mainly Mn_3O_4; however, when the size diminishes, the density of defects increases and

as a consequence γ-Mn_2O_3 (where all the manganese ions are Mn^{3+}) is the more stable shell phase. The systems exhibit exchange coupling between the core and the shell manifested by the exchange bias field and the large coercivity. Although the exchange field is strongly dependent on the magnetic anisotropy of the AFM core, we have observed (from the size dependence of the ESR line width) that while the magnetic anisotropy of the MnO core shows a smooth increase when the size is reduced, H_{ex} shows a nonmonotonic behavior. From neutron diffraction we have observed that the Néel temperature of the MnO core is substantially enhanced and that MnO presents an enhanced stability above T_N. The continuous magnetic phase transition in the AFM core is accompanied by the fragmentation−separation of the magnetic domains in smaller parts.

Supporting Information Available: Text giving the complete ref 88 and supplementary figures. This material is available free of charge via the Internet at http://pubs.acs.org.

JA1021798

(97) Catlow, C. R. A.; Fender, B. E. F. *J. Phys. C* **1975**, *8*, 3267–3279.